

# Light-Triggered Pyroelectric Nanogenerator Based on a pn-Junction for Self-Powered Near-Infrared Photosensing

Xingfu Wang,<sup>†,§,#</sup> Yejing Dai,<sup>†,#</sup> Ruiyuan Liu,<sup>†,#</sup> Xu He,<sup>†</sup> Shuti Li,<sup>§</sup> and Zhong Lin Wang<sup>\*,†,‡,§</sup>

<sup>†</sup>School of Materials Science and Engineering, Georgia Institute of Technology, Atlanta, Georgia 30332-0245, United States

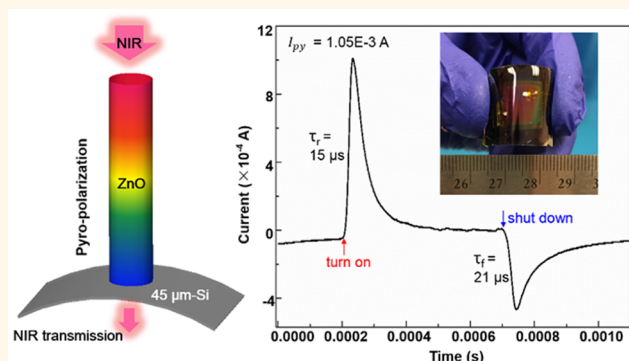
<sup>‡</sup>Beijing Institute of Nanoenergy and Nanosystems, Chinese Academy of Sciences, Beijing, China, 100083

<sup>§</sup>Laboratory of Nanophotonic Functional Materials and Devices, Institute of Optoelectronic Materials and Technology, South China Normal University, Guangzhou, China, 510631

## S Supporting Information

**ABSTRACT:** A nanogenerator, as a self-powered system, can operate without an external power supply for energy harvesting, signal processing, and active sensing. Here, near-infrared (NIR) photothermal triggered pyroelectric nanogenerators based on pn-junctions are demonstrated in a p-Si/n-ZnO nanowire (NW) heterostructure for self-powered NIR photosensing. The pyroelectric-polarization potential (pyro-potential) induced within wurtzite ZnO NWs couples with the built-in electric field of the pn-junction. At the moment of turning on or off the NIR illumination, external current flow is induced by the time-varying internal electric field of the pn-heterostructure, which enables a bias-free operation of the photodetectors (PDs). The NIR PD exhibits a high on/off photocurrent ratio up to  $10^7$  and a fast photoresponse component with a rise time of  $15\ \mu\text{s}$  and a fall time of  $21\ \mu\text{s}$ . This work provides an unconventional strategy to achieve active NIR sensing, which may find promising applications in biological imaging, optoelectronic communications, and optothermal detections.

**KEYWORDS:** pn-junction, pyroelectric nanogenerator, near-infrared, photosensing, self-powered



Near-infrared (NIR) light, as electromagnetic radiation with wavelengths between visible and infrared light, has a wide range of applications in biomedical imaging, remote temperature sensing, chemical analyzing, and environmental monitoring.<sup>1–3</sup> NIR sensing has attracted tremendous attention in the past few decades, and numerous NIR photodetectors (PDs) have been demonstrated based on a series of emerging material systems, such as nanocrystal quantum dots,<sup>4,5</sup> 2D layered materials,<sup>6,7</sup> and organolead halide perovskite.<sup>8,9</sup> The NIR photoabsorption capacities of these materials inherently limit the corresponding performances of the reported NIR PDs. More importantly, fundamentals of these PDs rely on the separation of photogenerated carriers by the built-in electric field formed within pn- and/or Schottky junctions. During this process, photoinduced voltage (PIV) arising from the separated carriers is formed with an opposite direction to the built-in electric field,<sup>10</sup> which can reduce the built-in electric field and weaken the separation of carriers in turn, thus limiting the photoresponse performances of NIR PDs. Therefore, NIR PDs with a rational design are highly

required to further improve their performances and expand their practical applications.

For pyroelectric materials with nonsymmetric structure, pyroelectric polarizations can be induced by time-dependently changing the temperatures across the material.<sup>11,12</sup> Furthermore, an IR radiation-induced change in temperature of the pyroelectric materials results in the generation of a pyroelectric-polarization potential (pyro-potential) along their polar direction.<sup>13</sup> In semiconductor devices formed with wurtzite ZnO nanowires (NWs), the introduction and existence of polarization potential (piezo-potential or pyro-potential) can effectively tune/control the charge movement/transport across the junction and modulate the optoelectronic processes of local carriers, leading to the emerging fields of piezo-tronics, piezo-phototronics, and pyro-phototronics. Moreover, a time-dependent change of the internal polarization electric field inside the ZnO NW(s) can effectively drive the flow of electrons through

Received: May 21, 2017

Accepted: August 2, 2017

Published: August 2, 2017



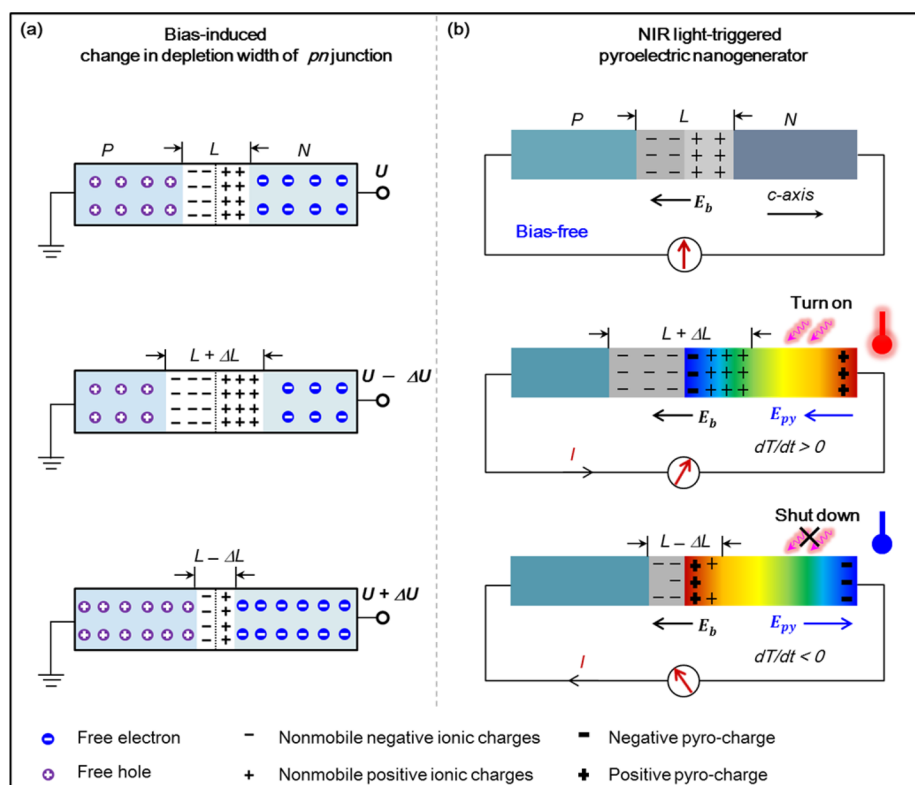


**Figure 1.** Working mechanisms of the light-triggered pn-junction-based pyroelectric nanogenerator. (a) A pn-junction is negatively biased under an external bias ( $U$ ), and the depletion width  $L$  is formed (upper). The depletion width will be expanded (upper) or shrunk (lower) if the external voltage increases or decreases, respectively. (b) A zero-biased pn-junction formed with p-Si and an n-ZnO NW, a depletion region (width of  $L$ ), and corresponding built-in electric field ( $E_b$ ) are formed (upper). Upon NIR illumination (middle), a transient high output current is generated and flows through an external circuit when  $dT/dt < 0$ . Upon shutting down the NIR light (lower),  $-E_{py}$  is produced, caused by  $dT/dt < 0$ , leading to a transient high output current in the reverse direction.

external circuits, and hence short-circuit current outputs are obtained. These are the fundamentals of pyroelectric and piezoelectric nanogenerators,<sup>11,14,15</sup> which have been revealed recently.<sup>16</sup>

The pn-junction is an important functional unit in today's electronics and optoelectronics. The depletion width and built-in electric field of the pn-junction dominant the transport properties of charge carriers and corresponding device performances. Normally, when a pn-junction is negatively biased under an external voltage of  $U$ , the depletion region with a width  $L$  is formed (Figure 1a, upper). The depletion width will be expanded ( $L + \Delta L$ ) or shrunk ( $L - \Delta L$ ) once the external voltage increases ( $U + \Delta U$ ) or decreases ( $U - \Delta U$ ), respectively, as shown in the middle and lower panel of Figure 1a. The variation of the depletion width is caused by the change of the built-in electric field. The expansion or shrinkage of the depletion region is equivalent to the increasing or decreasing of the built-in electric field inside the pn-junction.

The Maxwell displacement current, defined in terms of the rate of change of the electric displacement field, can be given by the equation<sup>16,17</sup>

$$J_D = \frac{\partial D}{\partial t} = \epsilon_0 \frac{\partial E}{\partial t} + \frac{\partial P}{\partial t} \quad (1)$$

where  $J_D$  represents the displacement current;  $D$  is the displacement field;  $E$  is the electric field, and  $\epsilon_0$  is the permittivity of a vacuum. As clearly illustrated previously,<sup>16,18</sup> the displacement current is not an electric current of moving free charges, but a *time-varying electric field* (vacuum or media).

Therefore, if the time-varying built-in electric field in a pn-junction is triggered by an ac stimulus under bias-free conditions, ac current flow in the external circuit can be induced by the displacement current inside the pn-junction. This is feasible to utilize to develop effective semiconductor devices for self-powered functional applications.

In this work, an NIR-light-triggered pyroelectric nanogenerator is demonstrated in a Si/ZnO NW pn-junction and is introduced to achieve self-powered NIR PDs. At the moment of turning on or off the NIR illumination, time varying of the total internal electric field (pyro-potential and built-in electric field) inside the pn-heterostructure results in the conductive current flow in the external circuit. Interestingly, the photo-response behavior of the NIR PD is tuned and the photoresponse performances are significantly improved by reducing the thickness of the p-Si substrate from 500  $\mu\text{m}$  to 45  $\mu\text{m}$ , which is attributed to the decreased PIV caused by the weakened photoabsorption in thinner Si devices. The 45  $\mu\text{m}$  ultrathin-Si-based NIR PD exhibits a higher on/off photocurrent ratio up to  $10^7$  and a better photoresponse component with a rise time of 15  $\mu\text{s}$  and a fall time of 21  $\mu\text{s}$ . The proposed working mechanisms of the self-powered NIR PD are further confirmed by fabricating and investigating the photoresponse properties and corresponding performances in three different types of NIR PDs: a Si/ZnO NW pn-junction devices, metal/ZnO NW Schottky-junction devices, and ITO/ZnO NW ohmic-junction devices.

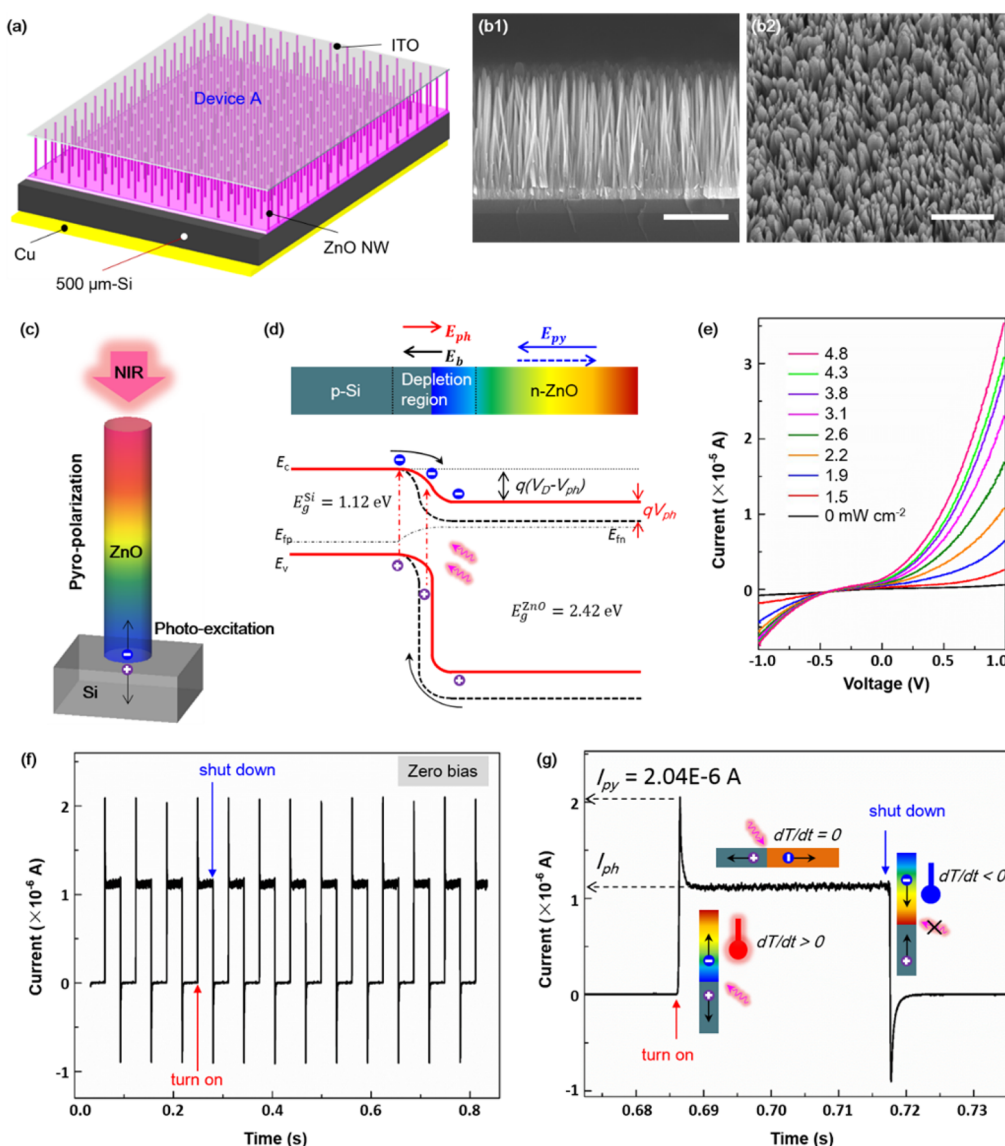


**Figure 2.** Structural and photoresponse characteristics of the NIR PDs based on the 500  $\mu\text{m}$  p-Si/n-ZnO NW heterostructure. (a) Schematic image of the 500  $\mu\text{m}$  p-Si/n-ZnO NW heterostructure devices. Cross-section-view (b1) and tilt-top-view (b2) scanning electron microscopy (SEM) images of the as-grown ZnO NWs, both with scale bars of 500 nm. (c) Upon the illumination of 1064 nm light, two optical processes are induced in the pn-junction device: the instantaneous pyro-polarization inside the ZnO NW and the photoexcitation at the local junction. (d) Photogenerated holes and electrons are separated, leading to the generation of  $E_b$ . (e)  $I$ - $V$  characteristics of the p-Si/n-ZnO NIR PDs under nine different power densities of NIR illumination. (f) Under bias-free conditions, the output-current response of the pn-junction PDs to 4.8  $\text{mW cm}^{-2}$  NIR illumination under periodical NIR illumination. (g) One typical cycle of the short-circuit  $I$ - $t$  curve.

## RESULTS AND DISCUSSION

The working mechanism of the NIR-light-triggered pyroelectric nanogenerator based on a pn-junction is schematically illustrated in Figure 1b. Considering a zero-biased pn-junction formed with a p-type nonpyroelectric semiconductor (e.g., p-Si) and an n-type pyroelectric semiconductor (e.g., n-ZnO NW), a depletion region (width of  $L$ ) with a built-in electric field of  $E_b$  is formed at the junction interface under thermal equilibrium conditions (Figure 1b, upper). If the polar  $c$ -axis of the ZnO NW points away from p-Si, upon NIR illumination (Figure 1b, middle), light-induced pyro-potential ( $E_{py}$ ) in the direction of  $E_b$  is created within the pyroelectric ZnO NW arising from the photothermal-induced instantaneous temperature increase ( $dT/dt > 0$ ) due to the superior photothermal heating property of NIR.<sup>19–21</sup> The depletion width is expanded by the  $E_{py}$  and

thus  $E_b$  increases. The total electric field inside the heterostructure ( $E_{\text{total}} = E_{py} + E_b$ ) increases instantly, and the time variation of  $E_{\text{total}}$  at this moment drives the flow of electrons through an external circuit and produces a transient short-circuit output current. The displacement current inside the pn-heterostructure results in the conduction current in the external circuit. Then the transient output current disappears and the current decreases to a steady-state value after the photothermal heating is stable and reaches equilibrium. This steady-state current is dominated by the optoelectric processes of the pn-junctioned devices, which will be discussed later. At the moment of shutting down the NIR light (Figure 1b, lower), a reverse pyro-potential ( $-E_{py}$ ) in the opposite direction of  $E_b$  is produced owing to the instantaneous temperature decrease ( $dT/dt < 0$ ). The depletion width is shrunk by the  $-E_{py}$  and  $E_b$  decreases. The total electric field ( $E_{\text{total}} = E_b - E_{py}$ ) decreases



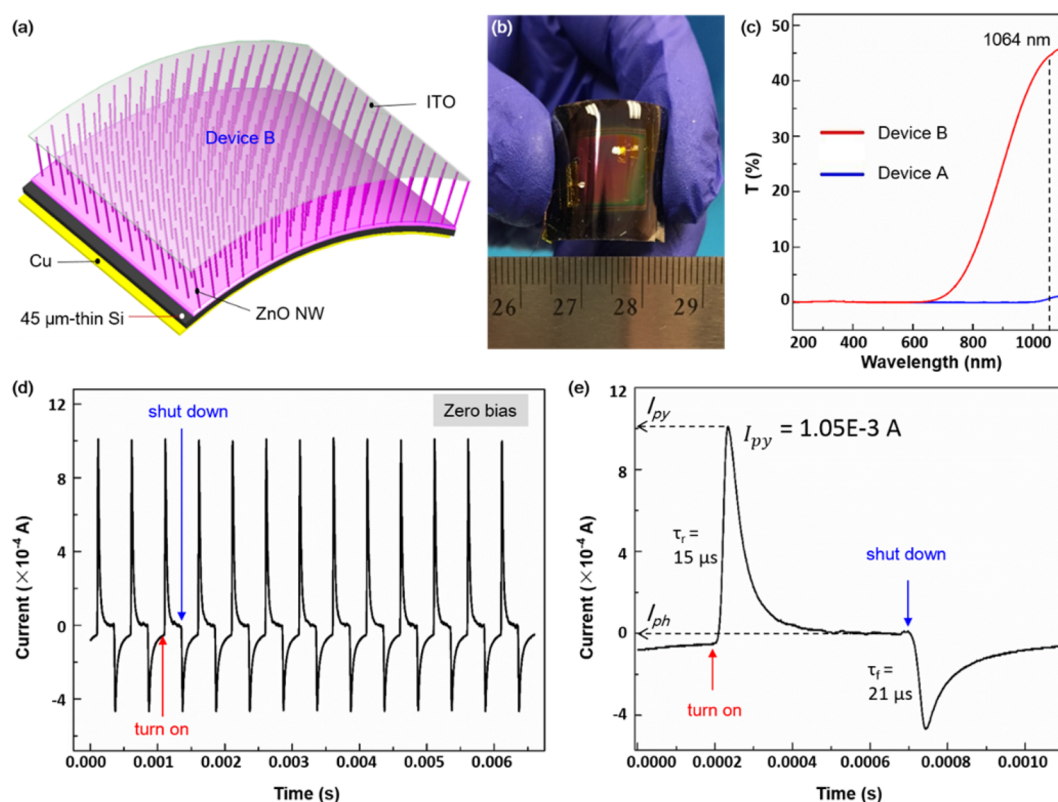


**Figure 3.** Schematic, digital images and photoresponse characteristics of the NIR PDs based on a 45  $\mu\text{m}$  p-Si/n-ZnO NW heterostructure. (a) Schematic and (b) digital images of the 45  $\mu\text{m}$  p-Si/n-ZnO NW heterostructure devices. (c) Transmission properties of the two different kinds of NIR PDs. (d) Under bias-free conditions, the output-current response of the pn-junction PDs to 4.8  $\text{mW cm}^{-2}$  NIR illumination under periodical NIR illumination. (e) One typical cycle of the short-circuit  $I$ - $t$  curve.

instantly, and the time-varying  $E_{\text{total}}$  at this moment drives the reverse flow of electrons through the external circuit and produces a transient short-circuit output current in the reverse direction. Last, the output current disappears and returns to a dark current after the photothermal heating vanishes. As clearly illustrated above, the transient current-output signals are generated without external bias at the moment of turning on and/or off the NIR light originating from the time-dependent NIR photothermal excitation; thus it is highly suitable for applications in effective and self-powered NIR photosensing.

In order to experimentally verify the proposed physical mechanisms and develop self-powered NIR photosensing of the pn-junction-based pyroelectric nanogenerator, p-Si/n-ZnO NW heterostructure devices (labeled as device A) were fabricated first by hydrothermally synthesizing uniform ZnO NWs on a 500- $\mu\text{m}$ -thick Si substrate, as schematically shown in Figure 2a. Cross-section-view and tilt-top-view scanning electron microscopy (SEM) images presented in Figure 2b1 and b2 indicate the as-grown ZnO NWs with average diameters of 30–60 nm and lengths of 800 nm. The detailed fabrication processes and measurement setup are found in the Methods section and the Supporting Information (Figure S1). Upon the illumination of NIR (1064 nm) from the ZnO side, two optical processes can be induced in the pn-junction device: the instantaneous pyropolarization inside ZnO NWs and the photoexcitation at the local junction caused by the photoabsorption of NIR in 500- $\mu\text{m}$ -thick Si (Figure 2c). Owing to the existence of  $E_b$  within the depletion region of the pn-junction, photogenerated holes and electrons will be separated and driven toward the p-Si and n-ZnO NWs side, respectively (Figure 2d). The separated

charge carriers lead to a photogenerated potential in the opposite direction to  $E_b$ . Therefore, the coupling among  $E_{\text{py}}$ ,  $E_{\text{ph}}$ , and  $E_b$  in the heterostructure devices can be expressed by  $E_{\text{total}} = E_{\text{py}} + E_b - E_{\text{ph}}$ , which dominates the photoresponse behavior and performances of the NIR PDs.

$I$ - $V$  characteristics of the p-Si/n-ZnO heterostructure device under a series of different power densities of NIR light illumination are measured and plotted in Figure 2e, showing good photoresponse properties of the NIR PDs. Under bias-free conditions, the output-current response of the pn-junction PDs to NIR illumination of 4.8  $\text{mW cm}^{-2}$  is systematically investigated and summarized in Figure 2f by periodically turning on and off the NIR light using an optical chopper. One typical cycle of the short-circuit  $I$ - $t$  curve extracted from Figure 2e is plotted in Figure 2f. It is clearly seen that a sharp current-response peak, with a magnitude of  $I_{\text{py}} = 2.04 \times 10^{-6}$  A, is induced at the moment the NIR light is turned on. This  $I_{\text{py}}$  is caused by the time-dependent change of the total electric field ( $E_{\text{total}}$ ) inside the pn-junctioned devices due to NIR-photothermal heating induced instantaneous temperature increase ( $dT/dt > 0$ ) in ZnO NWs, as clearly illustrated above. Then the pyro-potential is gradually reduced and disappears as the temperature variation vanishes ( $dT/dt = 0$ ) by retaining the power intensity of the NIR illumination, and the output current reaches a steady plateau ( $I_{\text{ph}}$ ) due to the stable separation of the photogenerated carriers by  $E_b$  within the depletion region. A reverse sharp current-response peak ( $-I_{\text{py}}$ ) is induced once the NIR light is turned off, originating from the reverse pyro-potential induced by the instantaneous temperature decrease ( $dT/dt < 0$ ) in the ZnO NWs. Last, the temperature returns to

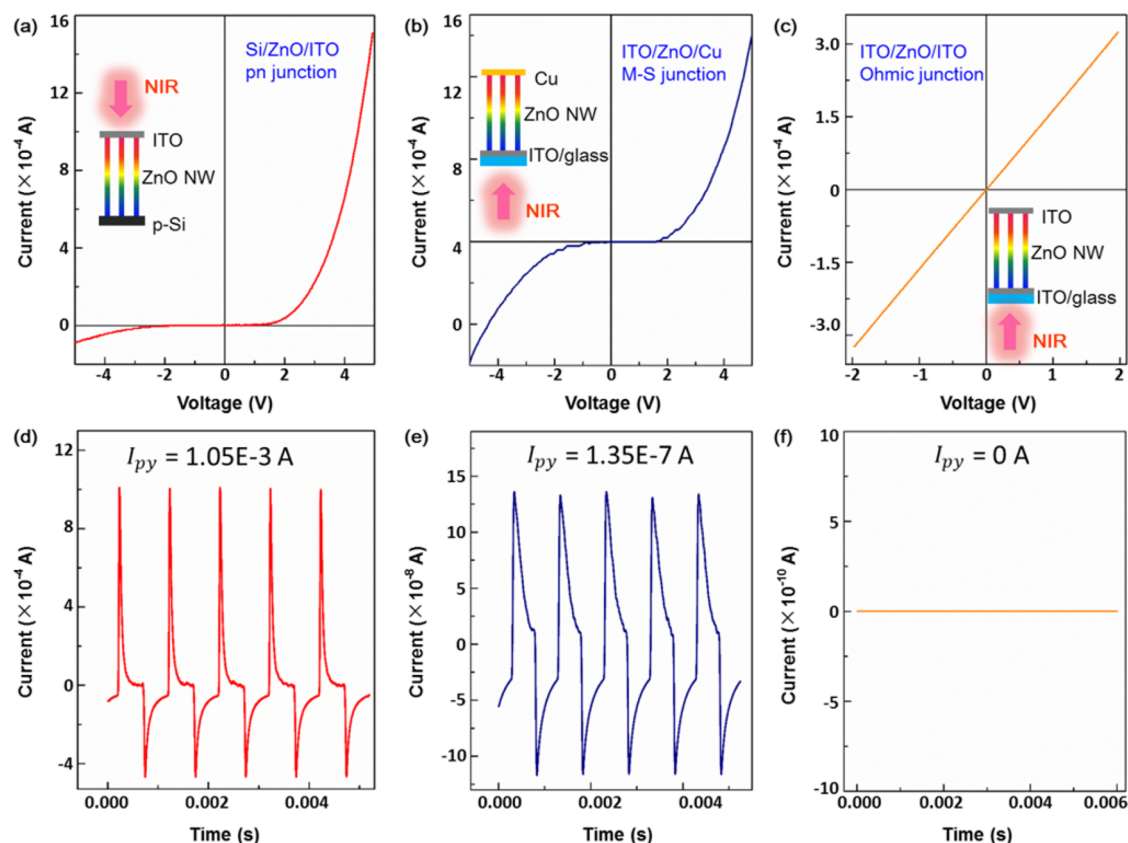


**Figure 4.** Schematic images,  $I$ – $V$  curves, and photoresponse properties of the pn-junction, Schottky-junction, and ohmic-junction devices.  $I$ – $V$  characteristics of the (a) pn-junction, (b) Schottky-junction, and (c) ohmic-junction devices, with corresponding schematic images of these three kinds of devices as inset images. The short-circuit photoresponse current of the (d) pn-junction, (e) Schottky-junction, and (f) ohmic-junction devices under periodical illumination of 1064 nm light.

room temperature and stays stable with the pyro-potential slowly vanishing again, and thus the output current returns to dark current. From the PD performances point of view, the photoresponsivity  $R$  is calculated as  $R = \frac{I_{py} - I_{dark}}{P_{ill}} = \frac{\eta_{ext} q}{h\nu} \gamma_G$ ,<sup>22,23</sup>

where  $P_{ill} = I_{ill} \times S$  is the NIR illumination power,  $\gamma_G$  represent the internal gain,  $\eta_{ext}$  is the external quantum efficiency,  $q$  is element electronic charge,  $h$  is Planck's constant,  $\nu$  is the frequency of light,  $I_{ill}$  is the excitation power density, and  $S$  is the effective area of the PDs. Under the NIR light power density of  $4.8 \text{ mW cm}^{-2}$ ,  $R$  is calculated to be  $4.3 \times 10^{-4} \text{ A W}^{-1}$ . Furthermore, the rising time is defined as the time from 10% to 90% of the maximum photocurrent, and the recovery time is defined as the falling time from 90% to 10% of the maximum photocurrent.<sup>24,25</sup> The response times of the self-powered p-Si/n-ZnO NW NIR PDs at the rising and falling edge are calculated to be 210 and 260  $\mu\text{s}$ , respectively.

To enhance the photoresponse performances of the NIR PDs, ultrathin-Si/ZnO NW pn-junction devices (labeled as device B) were fabricated by chemically reducing the thickness of the p-Si substrate from 500  $\mu\text{m}$  to 45  $\mu\text{m}$ . Details on the Si thickness-reduction processes are found in the Method section. The schematic and digital images of the 45  $\mu\text{m}$  ultrathin Si/ZnO NW based NIR PDs are shown in Figure 3a and b. Corresponding SEM images of the ultrathin-Si/ZnO NW heterostructure and the as-synthesized ZnO NWs are found in the Supporting Information (Figure S2). The transmission properties of devices A and B without a bottom Cu electrode are characterized and plotted in Figure 3c, indicating that the

transmittance of device B is much higher than that of device A at a wavelength of 1064 nm due to the thickness reduction. The significantly weakened NIR photoabsorption in device B will considerably reduce the amount of photogenerated carriers and corresponding  $E_{ph}$  component. The output-current response of device B to  $4.8 \text{ mW cm}^{-2}$  NIR illumination is measured under zero-biased conditions by periodically turning on and shutting down the NIR light with a 1000 Hz frequency, as plotted in Figure 3d. One typical cycle of the short-circuit  $I$ – $t$  curve is shown in Figure 3e. It is noteworthy that  $I_{ph}$  in device B is markedly decreased, on the order of  $10^{-10} \text{ A}$ , which is much lower than that in device A ( $10^{-6} \text{ A}$ ). Meanwhile, the induced sharp current-response peak at the moment the NIR illumination is turned on is as high as  $I_{py} = 1.05 \times 10^{-3} \text{ A}$ , exhibiting a high on/off photocurrent ratio up to  $10^7$ . The photoresponsivity  $R$  is calculated to be  $0.22 \text{ A W}^{-1}$ , which is nearly 3 orders of magnitude larger than that in device A. On the other hand, the response times of device B at the rising and falling edge are 15 and 21  $\mu\text{s}$ , corresponding to photoresponse speeds at the rising and falling edge 13.9 and 16 times faster than those in device A. The enhanced photoresponsivity and photoresponse speed of device B are attributed to the decrease of  $E_b$  and increased  $E_{total}$  (equal to  $E_{py} + E_b - E_{ph}$ ) upon the illumination of NIR light, as schematically shown in Figure S3 (Supporting Information).

One typical cycle of the short-circuit  $I$ – $t$  curve of the 45  $\mu\text{m}$  ultrathin Si/ZnO NW PDs under a series of different light frequencies is systematically investigated and summarized in Figure S4a (Supporting Information). Obviously, the induced

$I_{py}$  increases with increasing the light frequency, which is attributed to the enhanced temperature-change rate ( $dT/dt$ ) under higher light frequency conditions. The pyroelectric current can be described as  $I_{py} = P_c A(dT/dt)$ ,<sup>11,12</sup> where  $P_c$  is the pyroelectric current coefficient and  $A$  is the electrode area; therefore,  $I_{py}$  is proportional to  $dT/dt$ . The stability and durability of the pn-junction-based pyroelectric nanogenerator is also demonstrated by measuring hundreds of cycles of the short-circuit  $I-t$  curve of the 45  $\mu\text{m}$  ultrathin Si/ZnO NW PDs under a light frequency of 1 kHz, as shown in Figure S4b (Supporting Information). The systematical studies on the photoresponse properties of the 45  $\mu\text{m}$  ultrathin Si/ZnO NW NIR PDs and corresponding results also verify the physical mechanisms of the light-triggered pn-junction-based pyroelectric nanogenerator illustrated above. Compared with the convention photon NIR sensor, the demonstrated NIR sensor not only enables a self-powered operation but also benefits from its low-cost fabrication without involving complicated and expensive technology.

In order to further explore and confirm the origins of the induced current under zero-bias conditions, three different heterostructures of the devices were fabricated and studied: p-Si/n-ZnO NW pn-junction devices, n-ZnO NW/Cu Schottky-junction devices, and ITO/n-ZnO NW ohmic-junction devices.  $I-V$  characteristics of the pn-junction, Schottky-junction, and ohmic-junction devices, with corresponding schematic images of these three kinds of devices as inset images, are shown in Figure 4a, b, and c, respectively. The short-circuit photoresponse currents of these three different kinds of devices under periodical illumination of 1064 nm light are investigated and summarized in Figure 4d, e, and f. As clearly seen, the self-powered current is generated in pn-junction and Schottky-junction devices, while no current can be induced in ohmic-junctioned devices by periodically turning on and shutting down the NIR illumination. This can be attributed to the fact that the space charge region or depletion region exists only in the pn-junction and Schottky junction rather than at the ohmic junction;<sup>10</sup> therefore, the time-varying internal electric field inside the pn-junction and Schottky junction is significant, while the induced change of pyro-polarization is rapidly screened by the free electrons and holes inside the ZnO NWs. Moreover, the  $I_{py}$  induced in the pn-junction device at the moment the NIR light illumination is turned on is up to the order of  $10^{-3}$  A, which is nearly 4 orders of magnitude larger than that in Schottky devices ( $10^{-7}$  A). This agrees with the fact that the generated depletion region at the pn-junction interface is much larger than that in the Schottky junction, and hence the time-dependent variation of the built-in electric field induced by periodical NIR illumination in the pn-junction is more significant than that in the Schottky junction. These results consistently confirm the working mechanisms of the NIR-light-triggered pyroelectric nanogenerator based on a pn-junction.

## CONCLUSIONS

In conclusion, an NIR-light-induced pyroelectric nanogenerator based on a pn-junction is demonstrated in a p-Si/n-ZnO NW heterostructure, and a self-powered NIR PD is achieved. The photoresponse behavior of the NIR PD is tuned, and the photoresponse performances are significantly improved by reducing the thickness of the p-Si substrate from 500  $\mu\text{m}$  to 45  $\mu\text{m}$ , which is attributed to the reduced PIV due to the weakened photoabsorption in thinner Si devices. The 45  $\mu\text{m}$  ultrathin Si based NIR PD exhibits a high on/off photocurrent

ratio up to  $10^7$  and a superior photoresponse component with a rise time of 15  $\mu\text{s}$  and a fall time of 21  $\mu\text{s}$ . The proposed working mechanisms of the self-powered NIR PD are further confirmed by fabricating and measuring the photoresponse properties and performances in three different types of NIR PDs: Si/ZnO NW pn-junction devices, metal/ZnO NW Schottky-junction devices, and ITO/ZnO NWs ohmic-junction devices. This work provides an unconventional strategy to achieve active NIR sensing *via* an NIR-self-induced pyroelectric nanogenerator, which may find promising applications in optothermal detection, biological imaging, optoelectronic communications, and environmental monitoring.

## METHODS

**Fabrication Process of the 500  $\mu\text{m}$  p-Si/n-ZnO NW PDs.** A 500  $\mu\text{m}$  p-type Si wafer was purchased from UniversityWafer Inc. (100 mm B-doped (100) wafer, 1–10  $\Omega\text{ cm}$ , 500  $\mu\text{m}$  SSP prime). A ZnO seed layer was deposited by RF magnetron sputtering (PVD75, Kurt. J. Lesker Company) at a power of 120 W and chamber pressure of 8 mTorr for 30 min, with a thickness of 100 nm. The coated p-Si substrates were then placed into the mixed nutrient solutions (0.02 mM  $\text{Zn}(\text{NO}_3)_2$  and 0.02 mM hexamethylenetetramine) for ZnO NW growth *via* a hydrothermal method in a mechanical convection oven (model Yamato DKN400, Santa Clara, CA, USA) at 85  $^\circ\text{C}$  for 30 min. In order to get separated ZnO NWs and obtain the desired size, 5–10 mL of ammonium hydroxide (Sigma-Aldrich) was added per 100 mL of mixing solution. After cooling the whole system, the product was washed with ethanol and distilled water, collected, and vacuum-dried at 100  $^\circ\text{C}$  for 1 h. Then a thin layer of ITO was deposited on ZnO as the top electrode, and Cu was sputtered on the back of p-Si as a bottom electrode. Testing wires were connected to the top and bottom electrodes by silver paste. Finally, a thin layer of Kapton tape was applied to fix the testing wires and improve their robustness. Detailed microscopic structures of ZnO NWs are characterized by SEM (Hitachi SU8010).

**Fabrication Process of the 45  $\mu\text{m}$  p-Si.** A 500- $\mu\text{m}$ -thick Si wafer with a resistivity of 1–10  $\Omega\text{-cm}$  (University Wafer Inc.) was used to achieve the flexible Si substrate. The 4-in.-sized Si substrate was dipped into potassium hydrate (KOH) solution with a concentration of 50% at 130  $^\circ\text{C}$  for 6–8 h to be reduced to the desired thicknesses. The wafer became flexible when the thickness was in the scale of dozens of micrometers.

**Optical and Electrical Measurements.** Transmission spectra of ZnO were measured by a UV-vis spectrophotometer (JASCO V-630).  $I-V$  characteristics of the device are measured and recorded by a customized computer-controlled measurement system with a Stanford SRS low-noise current preamplifier (SR570)/SRS low-noise voltage preamplifier (SR560) in conjunction with a GPIB controller (GPIB-USB-HS, NI 488.2). The optical input stimuli were provided by a multichannel fiber coupled laser source (MCLS1, Thorlabs Inc.) with precisely adjustable light power density. The light power density used in this work was measured and obtained by a thermopile powermeter (Newport 818P-001-12). An NIR objective was used to expand the 1064 nm laser to illuminate the whole device in air at room temperature, and the effective size of the device is 10 mm  $\times$  10 mm.

## ASSOCIATED CONTENT

### Supporting Information

The Supporting Information is available free of charge on the ACS Publications website at DOI: 10.1021/acsnano.7b03560.

More detailed information about the schematic experimental setup; SEM images of the ultrathin-Si/ZnO NW devices; schematic image of the photoresponse within ultrathin-Si-based devices; frequency dependence on the photoresponse in the ultrathin-Si/ZnO NW PDs, and



corresponding stability demonstration of the NIR PDs (PDF)

## AUTHOR INFORMATION

### Corresponding Author

\*E-mail: [zhong.wang@mse.gatech.edu](mailto:zhong.wang@mse.gatech.edu).

### ORCID

Zhong Lin Wang: 0000-0002-5530-0380

### Author Contributions

\*X. Wang, Y. Dai, and R. Liu contributed equally to this work.

### Notes

The authors declare no competing financial interest.

## ACKNOWLEDGMENTS

Research was supported by the U.S. Department of Energy, Office of Basic Energy Sciences (Award DE-FG02-07ER46394).

## REFERENCES

- (1) Barone, P. W.; Baik, S.; Heller, D. A.; Strano, M. S. Near-Infrared Optical Sensors Based on Single-Walled Carbon Nanotubes. *Nat. Mater.* **2005**, *4*, 86–92.
- (2) Kim, S.; Lim, Y. T.; Soltesz, E. G.; De Grand, A. M.; Lee, J.; Nakayama, A.; Parker, J. A.; Mihaljevic, T.; Laurence, R. G.; Dor, D. M.; Cohn, L. H.; Mouni G Bawendi, M. G.; Cohn, L. H. Near-Infrared Fluorescent Type II Quantum Dots for Sentinel lymph Node Mapping. *Nat. Biotechnol.* **2004**, *22*, 93–97.
- (3) Chen, C. C.; Lin, Y. P.; Wang, C. W.; Tzeng, H. C.; Wu, C. H.; Chen, Y. C.; Chen, C. P.; Chen, L. C.; Wu, Y. C. DNA-Gold Nanorod Conjugates for Remote Control of Localized Gene Expression by Near Infrared Irradiation. *J. Am. Chem. Soc.* **2006**, *128*, 3709–3715.
- (4) Rauch, T.; Böberl, M.; Tedde, S. F.; Fürst, J.; Kovalenko, M. V.; Hesser, G.; Lemmer, U.; Heiss, W.; Hayden, O. Near-Infrared Imaging With Quantum-Dot-Sensitized Organic Photodiodes. *Nat. Photonics* **2009**, *3*, 332–336.
- (5) Saran, R.; Curry, R. J. Lead Sulphide Nanocrystal Photodetector Technologies. *Nat. Photonics* **2016**, *10*, 81–92.
- (6) Wang, L.; Jie, J.; Shao, Z.; Zhang, Q.; Zhang, X.; Wang, Y.; Sun, Z.; Lee, S. T. MoS<sub>2</sub>/Si Heterojunction with Vertically Standing Layered Structure for Ultrafast, High-Detectivity, Self-Driven Visible-Near Infrared Photodetectors. *Adv. Funct. Mater.* **2015**, *25*, 2910–2919.
- (7) Koppens, F. H. L.; Mueller, T.; Avouris, P.; Ferrari, A. C.; Vitiello, M. S.; Polini, M. Photodetectors Based on Graphene, Other Two Dimensional Materials and Hybrid Systems. *Nat. Nanotechnol.* **2014**, *9*, 780–793.
- (8) Dou, L.; Yang, Y. M.; You, J.; Hong, Z.; Chang, W. H.; Li, G.; Yang, Y. Solution-Processed Hybrid Perovskite Photodetectors with High Detectivity. *Nat. Commun.* **2014**, *5*, 5404.
- (9) Sutherland, B. R.; Johnston, A. K.; Ip, A. H.; Xu, J.; Adinolfi, V.; Kanjanaboos, P.; Sargent, E. H. Sensitive, Fast, and Stable Perovskite Photodetectors Exploiting Interface Engineering. *ACS Photonics* **2015**, *2*, 1117–1123.
- (10) Sze, S. M. Physics of Semiconductor-Devices. *CC/Eng. Technol. Appl. Sci.* **1982**, *27*, 28.
- (11) Yang, Y.; Guo, W.; Pradel, K. C.; Zhu, G.; Zhou, Y.; Zhang, Y.; Hu, Y. F.; Lin, L.; Wang, Z. L. Pyroelectric Nanogenerators for Harvesting Thermoelectric Energy. *Nano Lett.* **2012**, *12*, 2833–2838.
- (12) Yang, Y.; Wang, S.; Zhang, Y.; Wang, Z. L. Pyroelectric Nanogenerators for Driving Wireless Sensors. *Nano Lett.* **2012**, *12*, 6408–6413.
- (13) Batra, A. K.; Aggarwal, M. D. Pyroelectric Materials: Infrared Detectors, Particle Accelerators and Energy Harvesters. *USA: SPIE Press* **2013**, PM231, 22.
- (14) Maxwell, J. C. The Theory of Molecular Vortices Applied to Magnetic Phenomena. *Philosophical Magazine and Journal of Science*; London, Fourth series, p 161.
- (15) Wang, Z. L. On Maxwell's Displacement Current for Energy and Sensors: the Origin of Nanogenerators. *Mater. Today* **2017**, *20*, 74–82.
- (16) Jackson, J. D. *Electrodynamics*; Wiley-VCH Verlag GmbH & Co. KGaA, 1975.
- (17) Wang, Z. L.; Song, J. Piezoelectric Nanogenerators Based on Zinc Oxide Nanowire Arrays. *Science* **2006**, *312*, 242–246.
- (18) Lu, M. P.; Song, J.; Lu, M. Y.; Chen, M. T.; Gao, Y.; Chen, L. J.; Wang, Z. L. Piezoelectric Nanogenerator Using p-Type ZnO Nanowire Arrays. *Nano Lett.* **2009**, *9*, 1223–1227.
- (19) Ayala-Orozco, C.; Urban, C.; Knight, M. W.; Urban, A. S.; Neumann, O.; Bishnoi, S. W.; Shea, M.; Goodman, A. M.; Charron, H.; Mitchell, T.; Shea, M.; Roy, R.; Nanda, S.; Schiff, R.; Halas, N. J.; Joshi, A. Au Nanomaterials as Efficient Near-Infrared Photothermal Transducers for Cancer Treatment: Benchmarking Against Nanoshells. *ACS Nano* **2014**, *8*, 6372–6381.
- (20) Wang, S.; Riedinger, A.; Li, H.; Fu, C.; Liu, H.; Li, L.; De Donato, F. Plasmonic Copper Sulfide Nanocrystals Exhibiting Near-Infrared Photothermal and Photodynamic Therapeutic Effects. *ACS Nano* **2015**, *9*, 1788–1800.
- (21) Chou, S. S.; Kaehr, B.; Kim, J.; Foley, B. M.; De, M.; Hopkins, P. E.; Huang, J.; Brinker, C. J.; Dravid, V. P. Chemically Exfoliated MoS<sub>2</sub> as Near-Infrared Photothermal Agents. *Angew. Chem.* **2013**, *125*, 4254–4258.
- (22) Konstantatos, G.; Sargent, E. H. Nanostructured Materials for Photon Detection. *Nat. Nanotechnol.* **2010**, *5*, 391–400.
- (23) Wang, Z.; Yu, R.; Wang, X.; Wu, W.; Wang, Z. L. Ultrafast Response p-Si/n-ZnO Heterojunction Ultraviolet Detector Based on Pyro-Phototronic Effect. *Adv. Mater.* **2016**, *28*, 6880–6886.
- (24) Hatch, S. M.; Briscoe, J.; Dunn, S. A Self-Powered ZnO-Nanorod/CuSCN UV Photodetector Exhibiting Rapid Response. *Adv. Mater.* **2013**, *25*, 867–871.
- (25) Liu, X.; Gu, L. L.; Zhang, Q. P.; Wu, J. Y.; Long, Y. Z.; Fan, Z. Y. All-Printable Band-Edge Modulated ZnO Nanowire Photodetectors with Ultra-High Detectivity. *Nat. Commun.* **2014**, *5*, 4007.